Atmos. Meas. Tech., 9, 5103–5118, 2016
www.atmos-meas-tech.net/9/5103/2016/
doi:10.5194/amt-9-5103-2016

Atmospheric Measurement Techniques
Open Access
EGU

A five-channel cavity ring-down spectrometer for the detection of NO_2, NO_3, N_2O_5, total peroxy nitrates and total alkyl nitrates

Nicolas Sobanski, Jan Schuladen, Gerhard Schuster, Jos Lelieveld, and John N. Crowley

Atmospheric Chemistry Department, Max-Planck-Institut für Chemie, 55128 Mainz, Germany

Correspondence to: John N. Crowley (john.crowley@mpic.de)

Received: 31 May 2016 – Published in Atmos. Meas. Tech. Discuss.: 14 June 2016
Revised: 22 September 2016 – Accepted: 29 September 2016 – Published: 18 October 2016

Abstract. We report the characteristics and performance of a newly developed five-channel cavity ring-down spectrometer to detect NO_3, N_2O_5, NO_2, total peroxy nitrates (ΣPNs) and total alkyl nitrates (ΣANs). NO_3 and NO_2 are detected directly at 662 and 405 nm, respectively. N_2O_5 is measured as NO_3 after thermal decomposition at 383 K. PNs and ANs are detected as NO_2 after thermal decomposition at 448 and 648 K. We describe details of the instrument construction and operation as well as the results of extensive laboratory experiments that quantify the chemical and optical interferences that lead to biases in the measured mixing ratios, in particular involving the reactions of organic radical fragments following thermal dissociation of PNs and ANs. Finally, we present data obtained during the first field deployment of the instrument in July 2015.

1 Introduction

Nitrogen oxides play a central role in tropospheric chemistry though their influence on ozone production and radical cycling, and thus on the oxidative capacity of the atmosphere. Nitric oxide (NO) is directly emitted into the boundary layer by e.g. fossil fuel combustion and biomass burning, and is oxidised via various mechanisms (e.g. reaction with O_3 and peroxy radicals, RO_2) to form NO_2, which is the dominant precursor of photochemically formed, tropospheric ozone. Together, NO and NO_2 are referred to as NO_x, while the sum of all reactive, oxidised nitrogen species (NO_x plus inorganic and organic nitrates and nitrites and halogenated nitrogen oxides) is referred to as NO_y. In the tropospheric boundary layer, NO_2 mixing ratios vary from < 10 pptv in remote regions to > 100 ppbv in highly polluted environments. Tropospheric NO_2 has been measured using several techniques including differential optical absorption spectroscopy (DOAS), chemiluminescence (CLD), laser-induced fluorescence (LIF) and cavity ring-down spectroscopy (CRDS). For a summary and intercomparison of these methods, the reader is referred to Fuchs et al. (2010). NO_2 is the major precursor of the inorganic nitrates NO_3 and N_2O_5. During the daytime, NO_3 is rapidly photolysed (Johnston et al., 1996) and also reacts with NO to reform NO_2 so that NO_3 mixing ratios are very low. At night, NO_3 levels may reach hundreds of pptv in polluted air, and their reactions represent a significant route for oxidation of volatile organic compounds (VOCs) and, via formation of N_2O_5, are a source of particulate nitrate and thus sink of NO_x (Wayne et al., 1991; Allan et al., 1999). Tropospheric NO_3 has been detected using long-path DOAS (LP-DOAS; Platt et al., 1980) over a path length of typically > 1 km, whilst point detection methods of NO_3 include cavity-enhanced DOAS-, LIF- and CRDS-based instruments. N_2O_5 has been detected as NO_3 after thermal decomposition or directly measured by chemical ionisation mass spectrometry. Descriptions of methods for detecting NO_3 and N_2O_5 and an intercomparison experiment have recently been published (Fuchs et al., 2012; Dorn et al., 2013).

Reactions between atmospheric oxidants such as OH or NO_3 and anthropogenic or biogenic volatile organic compounds (VOCs) lead to the formation of organic peroxy radicals that react with NO or NO_2 to form organic nitrates (Roberts, 1990). Reaction of RO_2 with NO_2 results in the formation of peroxy nitrates (RO_2NO_2, henceforth abbreviated as PNs). If the initial peroxy radical contains a terminal acyl group ($R(O)O_2$), peroxyacetic nitric anhydrides

(also called peroxyacyl nitrates or PANs, $R(O)O_2NO_2$) are formed, which have lifetimes on the order of hours in temperate boundary layer conditions but weeks in cold regions of the atmosphere. Following generation and transport away from pollution sources, PANs can thermally decompose to NO_2 and an organic radical, thus providing NO_x and enhancing the production of O_3 in remote locations. Non-substituted peroxy radicals react to form PNs that are less thermally stable, which undergo rapid (timescale of seconds at 298 K) thermal decomposition in the mid-latitude boundary layer, and thus only reach higher concentrations in colder regions such as the upper troposphere and regions close to the poles (Slusher et al., 2002; Murphy et al., 2004). The reaction of RO_2 with NO mainly forms RO + NO_2, but can also result in the formation of alkyl nitrates ($RONO_2$, henceforth abbreviated as ANs) in a minor branch (1–30 %) of this reaction, with higher yields for long-chain peroxy radicals (Arey et al., 2001; Perring et al., 2013). ANs are also formed at night from the reaction between NO_3 and VOCs with a higher yield (20–80 %) than the OH-initiated process (Perring et al., 2013). The oxidation of alkenes by NO_3 results in the formation of nitroxy alkyl radicals that can react with O_2 to form nitroxy alkyl peroxy radicals that can undergo further chemistry. ANs are longer lived than PANs against thermal decomposition, and can thus also act as NO_x reservoirs. Reactions with OH or photolysis or transfer to the aerosol phase are the major sinks of ANs, the relative importance depending on carbon chain size and degree of substitution. PNs and ANs represent a very wide group of species present in the atmosphere, with different levels of structural complexity due to the different possible combinations of functional groups. Individual nitrates can be measured using chromatography-based instruments followed by electron capture detection, conversion to NO or NO_2 (Roberts et al., 1989; Roberts, 1990; Flocke et al., 1991; Blanchard et al., 1993) or chemical ionisation mass spectrometry (Beaver et al., 2012), whereas the detection of the total (i.e. non-speciated) ambient PNs and ANs has been demonstrated using thermal decomposition of the nitrates followed by NO_2 detection (Day et al., 2002, 2003; Paul et al., 2009; Paul and Osthoff, 2010; Wooldridge et al., 2010; Thieser et al., 2016).

A single instrument that measures NO_2, NO_3, N_2O_5, total peroxy nitrates (ΣPNs) and total alkyl nitrates (ΣANs) can clearly provide great insight into the reactive nitrogen budget of the troposphere, enabling studies of daytime and night-time processes that transfer NO_x from the gas to the particle phase or to organic reservoir species. The interconversions and relation to NO_x losses and photochemical O_3 generation of these traces gases are described in Fig. 1, and those highlighted in red circles are detected with this instrument. The five-channel instrument we describe is a further development and extension of the two-channel, one-colour (405 nm) prototype recently described by Thieser et al. (2016) and of the two-channel set-up for measuring NO_3 and N_2O_5 previously developed and operated by this group

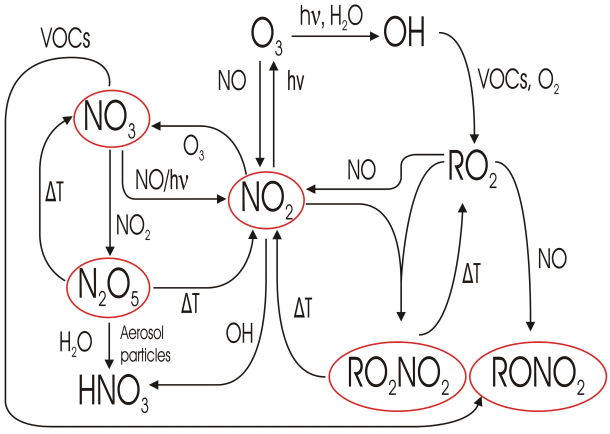

Figure 1. Atmospheric sources and sinks of the NO_y species (in red circles) measured by the five-channel TD-CRDS instrument described in this work and their link to VOC degradation and photochemical O_3 formation.

(Schuster et al., 2009). Whilst some basic concepts are similar, several significant design modifications (optical, mechanical, electrical/data-acquisition and chemical) have been made that improve the precision, the limit of detection and the accuracy of the measurements. These improvements are described in the relevant sections below.

In Sect. 2 we describe the overall design of the instrument and the features specific to the measurement of the individual trace gases. In Sect. 3 calibration procedures and laboratory characterisation experiments are described, along with an assessment of the overall uncertainty. Finally, in Sect. 4 we show data from a first field deployment at a semi-rural mountain site in Germany.

2 Instrument design

The instrument we describe uses cavity ring-down spectroscopy (CRDS), partly coupled with thermal dissociation (TD-CRDS). CRDS is a detection technique that was developed in the early 1990s (O'Keefe and Deacon, 1988; Lehmann and Romanini, 1996), and has been recently reviewed (Berden et al., 2000; Brown, 2003). The underlying principle of CRDS is the measurement of optical extinction in a (usually) closed cavity. In contrast to differential absorption spectroscopy in which optical extinction is linked to a measured light intensity difference, in CRDS set-ups, the optical extinction is calculated from the rate of decay of light intensity (ring-down constant) measured at the output of the cavity after a light pulse (pulsed CRDS) or after a continuous light source is turned off (cw-CRDS). The light intensity decay, measured behind a cavity mirror after switching the light source off, is exponential, and the concentration of an

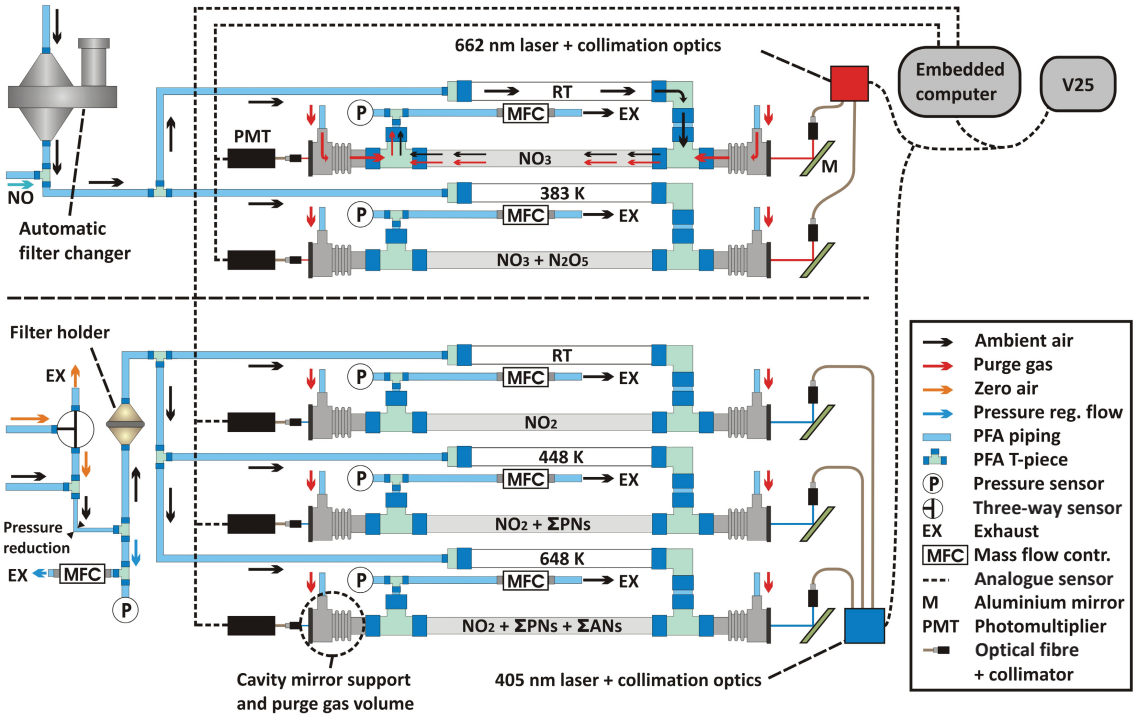

Figure 2. Schematic of the five-channel TD-CRDS. Gas flows are represented by coloured arrows. The wall temperatures of the different inlets are given for each channel. RT: room temperature.

absorbing/scattering gas (i) can be calculated using Eq. (1):

$$[i] = \frac{1}{c\sigma_{(i,\lambda)}}\left(\frac{1}{\tau(s)} - \frac{1}{\tau_0}\right), \quad (1)$$

where τ_0 and τ (s) correspond to decay constants in the absence and presence of absorbing/scattering trace gases, respectively (see Sect. 2.1 and 2.2). $\sigma_{(i,\lambda)}$ is the absorption cross section/scattering coefficient of species i at wavelength λ. The determination of the decay constants is done using a linear regression of sums fitting method (LRS), which has a number of advantages compared to least-squares (LS) fitting (Everest and Atkinson, 2008), including a faster algorithm and the removal of the need to measure an accurate zero (or baseline), which enables use of shorter on–off modulation cycles and higher data acquisition frequencies. Comprehensive comparison between the LS and LRS methods for both synthetic and real ring-down decays showed excellent agreement.

The central part of the instrument described here consists of five cavities of similar design and materials (see Fig. 2). Two cavities are used to detect NO_3 and N_2O_5 (at 662 nm), and three are used to detect NO_2, ΣPNs and ΣANs (at 405 nm). We refer to the five different inlet/cavity combinations (downstream of the filters, see Fig. 2) as the NO_2, NO_3, N_2O_5, ΣPNs and ΣANs channels. The light sources for the five cavities are two laser diodes housed in Thorlabs TCLDM9 modules located in aluminium housing with optical components for beam splitting, collimation and optical isolation (see Sect. 2.1 and 2.2). Coupling between the laser diodes and the cavities is achieved using 50 µm core optical fibres with collimators adjusted to weakly focus the beam (diameter of ≈3 mm) at a point ≈1 m behind the cavity output mirrors. The cavities are constructed from 70 cm long, seamless stainless-steel pipes (1 mm thick, with an inner diameter of 8 mm), which are Teflon-coated (DuPont, FEP, TE 9568). The use of stainless steel as cavity material is considered superior to glass, as used in our previous set-ups (Schuster et al., 2009; Thieser et al., 2016) as it eliminates the risk of breakage, and provides more homogeneous heating of the cavities. Radical losses on FEP-coated stainless-steel or glass surfaces are indistinguishable. PFA T-pieces (Swagelok) are mounted at both ends of the piping for admitting and exhausting the sample flow. Metal bellows/adjustable mirror supports are positioned behind each T-piece, resulting in a distance between mirrors of 93 cm. The bellows provide a purge gas volume for keeping the mirrors clean and reducing physical stress on the mirror supports. The 10 cavity mirrors are continuously purged with dry, synthetic air to prevent degradation in reflectivity. Purging the mirrors has the drawback of reducing the effective cavity length, and thus sensitivity, but it enabled uninterrupted operation over periods of several months. The 10 different purge gas streams are controlled by two mass flow controllers coupled with two sets of crit-

ical orifices designed for different purge flow rates depending on the size and direction of flow of ambient air through the cavities. The purge gas flows for the 405 nm cavities are 500 cm^3 (STP) min^{-1} (sccm) for the mirror opposing the main gas flow (downstream) and 100 sccm for the upstream mirror. For the 662 nm cavities, these flows are 350 (downstream) and 150 sccm (upstream). The light intensity exiting each cavity is measured and converted to an analogue electric signal by a photomultiplier/preamplifier device (Hamamatsu H10492-012 at 662 nm and H10492-002 at 405 nm). Temperature, pressure and flows are measured/regulated by a custom-designed control unit (referred to as V25). Data acquisition (ring downs and laser spectra) and data processing are performed by an embedded computer (NI PXIe-8135). Analogue-to-digital conversion of the photomultiplier signals is performed via two acquisition cards (NI PXI-6132, 14 bit, 3 MS s^{-1}) in the embedded computer rack, one for the two 662 nm cavities and one for the three 405 nm cavities.

2.1 Detection of NO_3 and N_2O_5 at 662 nm

NO_3 and N_2O_5 are detected using the strong absorption feature of NO_3 at about 662 nm ($\sigma_{662\,nm} \approx 2.3 \times 10^{-17}$ cm^2 $molecule^{-1}$ at 298 K; Orphal et al., 2003; Osthoff et al., 2007). NO_3 is measured in one channel (the NO_3 channel) at room temperature. In a second channel (the N_2O_5 channel), the sum of ambient NO_3 and NO_3 arising from the thermal decomposition of N_2O_5 at 383 K are measured, enabling the N_2O_5 mixing ratio to be calculated from the difference. The cavity mirrors (Advanced Thin Films, 1 in. diameter, 1 m radius of curvature) have a nominal reflectivity of 0.999985 and result in ring-down times (at atmospheric pressure of dry synthetic air) of 150–160 µs. To keep a constant emission wavelength of ≈ 662 nm, the laser diode (Thorlabs HL6545MG) is thermostatted to 38 °C and has an emission bandwidth of ≈ 0.5 nm (full width half maximum). An optical isolator is positioned at the immediate output of the diode laser to prevent back reflexions, and the final intensity of light reaching the front mirror of each of the two red cavities is ≈ 10–15 mW. The laser wavelength is monitored using a mini spectrograph (Ocean Optics, type HR4C2509), which records diffuse back reflexions from the N_2O_5 cavity input mirror. Taking into account the emission spectrum and the absorption cross section of NO_3, the effective cross section obtained during the first field deployment and calibrations is $\approx 2.1 \times 10^{-17}$ cm^2 $molecule^{-1}$. The uncertainty on the effective cross section is discussed in Sect. 3.1.

Before entering the NO_3 and N_2O_5 channels, air (≈ 15 L (STP) min^{-1}, slm) is drawn through a filter (Pall Corp., Teflon membrane, 47 mm ∅, 0.2 µm pore) housed in an automatic filter changer. The changer has a maximum capacity of 20–25 filters, allowing for 2–3 nights of measurement (at a change rate of one filter per hour) without requiring the presence of an operator. Losses of NO_3 in the filter and filter changer are discussed in Sect. 3.1. Air exits the filter changer through a 1/4 PFA pipe (≈ 30 cm) with a T-piece to enable the injection of a few standard cubic centimetres per minute of NO (100 ppmv in N_2) for titrating NO_3 and zeroing the instrument, which was performed for a few seconds every 4 min. The air then passes through another T-piece that divides the flow between the NO_3 (8 slm) and N_2O_5 (7 slm) channels. For N_2O_5 detection, the air flows through a heated Teflon-coated glass section (wall temperature 383 K) to decompose N_2O_5 into $NO_3 + NO_2$. This temperature is sufficient to decompose all the N_2O_5, which was verified experimentally by increasing the temperature until the maximum signal was obtained. The residence time in this reactor (≈ 0.2 s) is sufficient to allow for a reaction between total NO_3 and NO to go to completion during zeroing periods. In the NO_3 channel, the air flows first though FEP-coated glass tubing at room temperature to ensure sufficient time for complete NO_3 titration when adding NO (i.e. when zeroing). Residence times are 0.45 s in the NO_3 channel and 0.38 s in the N_2O_5 channel. The pressure in the NO_3 and the N_2O_5 channels is not regulated, and it depends on atmospheric pressure and flow rates in the instrument.

A square-wave signal provided by the V25 is used to modulate the diode laser on and off, and also triggers the acquisition of the individual decays. Typically, the modulation frequency is 400 Hz, with on and off times of 1 and 1.5 ms. Averaging 400 decay constants thus resulted in an instrumental time resolution of one data point per second. An Allan deviation plot obtained under laboratory conditions (800 mbar cavity pressure) for the NO_3 and N_2O_5 cavities is shown in Fig. 3. The Allan deviation plot shows that the (1σ) standard deviations of the zero signal (obtained in this experiment by sampling zero air) for the NO_3 and N_2O_5 channels for a 1 s integration time are 0.1 and 2 pptv, respectively. This is found to be a significant improvement in signal-to-noise ratio compared to the instrument described by Schuster et al. (2009), for which 5 s integration times were necessary to reduce noise levels to ≈ 2 pptv for both NO_3 and N_2O_5 channels. The improvement is likely related to the more stable optical set-up. Despite the fact that the two 662 nm channels in the new instrument are mechanically and optically very similar, the N_2O_5 channel shows a higher noise level, which is related to enhanced turbulence due to temperature and thus density gradients.

2.2 Detection of NO_2, ΣPNs and ΣANs at 405 nm

Three channels sampling in parallel are used for the detection of NO_2 and organic nitrates. The three cavities are maintained at slightly above ambient temperature (305 K) to reduce density fluctuations. All three channels detect NO_2 (ambient, or produced by organic nitrate decomposition) using the absorption of NO_2 at 405 nm (σ_{405nm} at 298 K $\approx 6 \times 10^{-19}$ cm^2 $molecule^{-1}$; Voigt et al., 2002). The cavity mirrors (Advanced Thin Films) have a reflectivity $R \approx$ 0.99995, which results in an average ring down of 30–35 µs

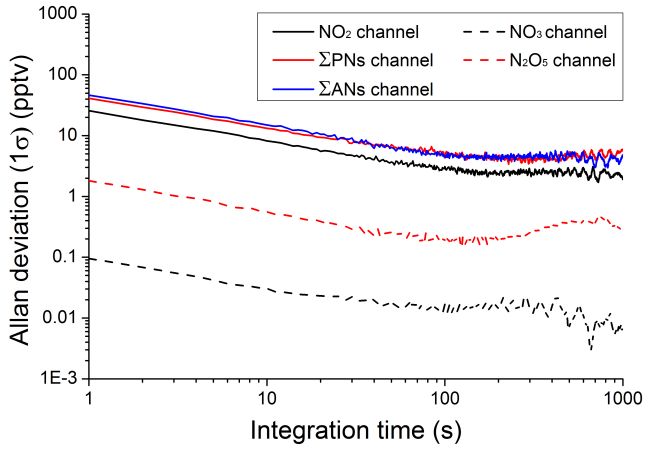

Figure 3. Allan deviation plot (1σ) for each of the five CRDS channels. The data were obtained in the laboratory at ≈ 298 K and a cavity pressure of 800 mbar.

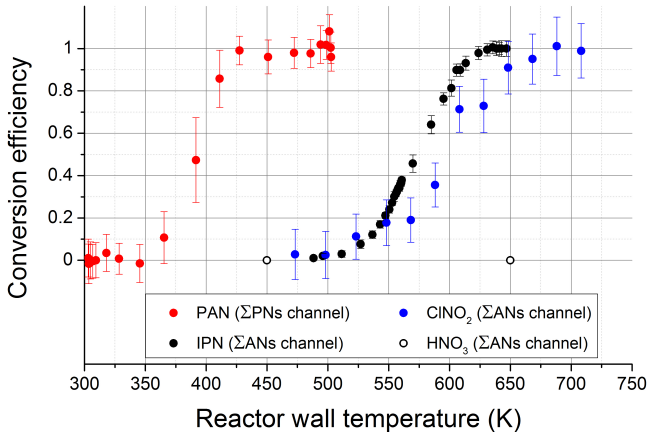

Figure 4. Decomposition profiles of PAN (red points), i-propyl nitrate (black points) and $ClNO_2$ (blue points) with statistical errors (1σ). The PAN decomposition profile was measured in the ΣPNs channel; the i-propyl nitrate (IPN) and $ClNO_2$ profile were measured in the ΣANs channel. The open black circles indicate the lack of HNO_3 decomposition when sampled into the ΣANs channel.

at 700 mbar of dry synthetic air. The 405 nm cavities have a data acquisition system and optical set-up that is similar to the 662 nm cavities, although an optical isolator to prevent back reflections was found by empirical observation to be unnecessary at 405 nm. To keep the peak emission wavelength at 405 nm, the laser diode is held at 35 °C. The maximum intensity coupled into each of the three 405 nm cavities is in the range 10–15 mW. The laser wavelength is monitored using a mini spectrograph (Ocean Optics, type HR4C5451), which records diffuse back reflexions from the ΣANs cavity input mirror. The effective cross section for the three 405 nm channels during the calibrations and field deployment was 5.9×10^{-19} cm^2 molecule^{-1} (based on the laser emission spectrum and the NO_2 absorption cross section).

Ambient NO_2 is detected directly when sampling from a room temperature inlet, whereas PNs and ANs are thermally decomposed in two heated sections of glass tubing at ≈ 448 and ≈ 648 K and then detected as NO_2. In the 448 K channel (ΣPNs channel), the sum of ambient NO_2 plus NO_2 from the thermal decomposition of PNs is measured. In the 648 K channel (ΣANs channel), NO_2 from the decomposition of ANs is additionally detected. The temperature set in the ΣPNs channel (448 K) was chosen by measuring the temperature dependence of the thermal dissociation of PAN (≈ 2 ppbv) in synthetic air as provided by a diffusion source of PAN in tridecane. The normalised [NO_2] signal as a function of temperature (Fig. 4) shows that complete decomposition to NO_2 is achieved at a nominal temperature of ≈ 433 K. The temperatures given in the text and in Fig. 4 correspond to the external surface of the heated inlets and not necessarily that of the gas flowing through them. PANs have a thermal stability that is largely independent of the *R* group (Roberts, 1990; Kirchner et al., 1999). For the detection of atmospheric PNs, we set the temperature to 15 K above the threshold measured in the laboratory for PAN, i.e. 448 K. Figure 4 also shows the temperature-dependent decomposition of a sample of isopropyl nitrate in synthetic air: a yield of 100 % is reached at a set temperature of ≈ 633 K. As for PANs, the thermal decomposition of all ANs is expected to be similar, so a working temperature of 648 K was chosen.

Rayleigh scattering of 405 nm light by air (Fuchs et al., 2009; Thieser et al., 2016) results in sensitivity of the ring-down constant to pressure changes, and requires that the three 405 nm cavities are actively pressure-regulated. For this reason, and because zeroing requires overfilling the inlet line (see below), the 405 nm channels have an independent inlet system. In total, ≈ 8 slm air is sampled through 1/4 in. PFA piping, of which 0.5 slm is directed to a digital humidity sensor. Active pressure control of the cavities is achieved by pumping a regulated fraction of the main flow (usually ≈ 0.5 slm) through a flow controller directly to the exhaust system (see Fig. 2) to maintain the desired pressure (generally about 700 mbar). About 7 slm of ambient air is drawn through a filter held by a PFA filter holder. The particle filters used to protect the 405 nm cavities are the same as for the 662 nm cavities, but are changed at a much lower frequency (once per day per hand) due the lower reactivity of NO_2 and organic nitrates to surfaces. After passing through the particle filter, air is then split into three equal flows (≈ 2.3 slm), resulting in residence times of 1.7, 1.3 and 1.1 s for the NO_2, ΣPNs and ΣANs channels, respectively. The three 405 nm channels consist of vertically mounted glass tubing (length ≈ 55 cm, ID = 12 mm) connected to the cavities by PFA fittings as described in Sect. 2. For the ΣPNs and ΣANs channels, a portion of the glass tubing is wrapped with heating wire and heavily insulated to achieve the desired thermal dissociation temperatures of 448 and 648 K. The first 10 cm of the heated section of the glass tubing in the ΣPNs and

ΣANs channels is filled with glass beads (≈ 0.5 mm diameter, Sigma-Aldrich G9268) supported on a glass frit (ca. 2 cm long). More detail and a diagram is given in the Supplement. The surfaces of the glass beads and glass frit scavenge organic radicals formed in the thermal decomposition of PNs and ANs, and thus reduce the impact of radical recombination with NO_2 and oxidation of NO, which can bias the results obtained, especially under conditions of high NO_x (Day et al., 2002; Paul and Osthoff, 2010; Thieser et al., 2016). Details of the laboratory experiments carried out and the corrections necessary to take such processes into account are described in Sect. 3.2.

The three 405 nm channels are zeroed for 30 s every 4 min by overflowing the inlet with ≈ 0.2 slm of bottled synthetic air or with scrubbed air provided by a zero-air generator (CAP 180, Fuhr GmbH). An upper limit to the NO_2 content of the zero air of ≈ 20 pptv was obtained by use of a blue-light converter, as described previously (Thieser et al., 2016). Previous work has shown that the different scattering coefficients for humid, ambient air and the dry, synthetic air used to zero the instrument can lead to a bias in the measured [NO_2]. The difference in the Rayleigh scattering cross section at wavelengths close to 405 nm between synthetic air and water ($\Delta\sigma$) is reported to be between 0.4 and 0.5×10^{-21} cm^2 molecule^{-1} (Fuchs et al., 2009; Thieser et al., 2016). At 50–60 % humidity at 30 °C and 1 bar, this results in an offset of ≈ 200 pptv in the [NO_2] signal. Thieser et al. (2016) have indicated that the 20 % difference in the reported scattering cross sections renders this a significant source of uncertainty at high relative humidity and low NO_2. To avoid introducing additional error by correcting for this, we implemented a zero-air humidification system, which enables the 7 slm air flow used for zeroing the instrument to be actively matched (to better than 2 % up to 80 % relative humidity; RH) to ambient RH (of ambient and zero-air, both measured at 0.2 Hz). This was achieved by passing a variable fraction of the zero air to a bubbler containing distilled water. Taking $\Delta\sigma = 0.5 \times 10^{-21}$ cm^2 molecule^{-1}, the error arising for a 2 % humidity difference at room temperature and 1 bar (measuring conditions of both humidity sensors) is equal to 10 pptv.

As the ring-down times are shorter at 405 nm (typically 35 µs), the diode laser modulation frequency could be increased so that 1666 ring-down constants were obtained per second. Figure 3 shows an Allan deviation plot (1σ) for the NO_2, ΣPNs and ΣANs channels. The 1σ standard deviations for a 1 s integration time for the three 405 nm channels are 25, 40 and 45 pptv, respectively. The higher noise level associated with the ΣPNs and ΣANs channels results from slightly lower mirror reflectivity (different batch) compared to the NO_2 cavity.

3 Data corrections, precision and total uncertainty

When based on known absorption cross sections, CRDS is an absolute concentration measurement technique. However, a number of corrections are necessary to convert measured ring-down times into volume mixing ratios of absorbing trace gases. Some corrections are related to the physical construction of the cavities, and others are related to chemical processes in the inlets and cavities that can bias the concentrations measured. The size and accuracy of these corrections contribute significantly to the overall uncertainty of the measurements, and are discussed in detail below. The more straightforward corrections needed are related to the effective absorption path length (l-to-d ratio), losses of NO_3 radicals in inlets and filters as previously described (Schuster et al., 2009; Thieser et al., 2016) and formation of NO_2 during the sampling time through $O_3 + NO$ reaction. For this instrument, the effective l-to-d ratio is 0.69 ± 0.02 for the channels detecting at 405 nm, and 0.77 ± 0.04 for the channels detecting at 662 nm. Based on several laboratory experiments, the transmission of NO_3 in the filter/filter holder is 70 ± 3 %. The 3 % uncertainty was obtained by repeated measurements under laboratory conditions. During the NOTOMO campaign (see Sect. 4), no discontinuities in the NO_3 signal were observed after hourly filter changes, which implies that there was no measurable change in transmission over the hour of exposure. In highly polluted environments, or those with highly reactive aerosol, this may not be the case, and more frequent filter changes may be necessary to avoid loss of NO_3. No losses of N_2O_5 on passage through the filter holder are observed under laboratory conditions, and similarly to NO_3, no evidence was obtained for losses on aged filters during the NOTOMO campaign. The transmission of NO_3 in the NO_3 and N_2O_5 channels is 97.4 ± 2.5 % and 90.2 ± 5 %, respectively. Details and results of the experiments to derive l-to-d ratios and correction factors for NO_3 losses are given in the Supplement. Corrections related to NO oxidation by O_3 are described in Sect. 3.2.5.

3.1 NO_3 and N_2O_5 channels

For averaging periods of longer than ≈ 1 s, the detection limit of both [NO_3] and [N_2O_5] is defined mainly by variation/drift in the zero signal. Drifts can arise from changes in the mirror reflectivity and through thermal and mechanical stresses that influence the cavity alignment. The detection limit can be estimated by the 2σ standard deviation of the difference from one zeroing period to the next one for the whole campaign. The values for the NO_3 and N_2O_5 channels are respectively 1.5 and 3 pptv, and imply that 95 % of the time, the difference between one zero value to the next one is lower than 1.5 and 3 pptv respectively. The NO_3 limit of detection is thus 1.5 pptv for 1 s averaging and zeroing every 3 min. As N_2O_5 is obtained by difference, the detection limit is ≈ 3.5 pptv (also for 1 s averaging). The total uncertainty

for the [NO_3] measurement can be estimated by propagation of the individual uncertainties associated with the correction factors (see above) and the uncertainty associated with the effective absorption cross section, which depends on the NO_3 absorption cross section uncertainty ($\approx 10\,\%$, taken from Osthoff et al., 2007) and the uncertainty associated with measurement of the laser emission spectrum ($\approx 5\,\%$). The resulting total uncertainty for NO_3 measurement is 25 %. The uncertainty associated with the [N_2O_5] measurement depends on the absolute values of [NO_3] and [N_2O_5], and is therefore variable. As an example, combining the 25 % uncertainty of the total NO_3 measured in the N_2O_5 channel with [NO_3] and [N_2O_5] mixing ratios of 50 and 500 pptv results in an uncertainty of 28 % for the N_2O_5 measurement.

3.2 NO_2, ΣPNs and ΣANs channels

3.2.1 Losses of NO_2 in the heated ΣPNs and ΣANs inlets

The transmission of NO_2 through the hot glass inlets (with frit and packed with glass beads) of the ΣPNs and ΣANs channels was investigated by sampling NO_2 in synthetic air (up to 10 ppbv) into the three 405 nm channels simultaneously. NO_2 is depleted slightly in the hot inlets with a transmission of 98.5±2 % and 95.5±2 % found for the ΣPNs and ΣANs inlets, respectively (see Fig. 5). The NO_2 transmission was measured before, during and after the field deployment of this instrument (corresponding to a period of several months), and was found to be constant and also independent of relative humidity.

3.2.2 Reaction of radicals with NO / NO_2 in the ΣPNs channel (448 K)

The thermal decomposition of PNs leads to the formation of organic radicals and NO_2. In an ideal situation, in which PNs decompose 100 % to NO_2 and when NO_2 does not undergo any further production or loss reaction, the total [NO_2] measured in the ΣPNs channel is equal to the sum of ambient NO_2 and PNs. Under the operating conditions of the CRDS instrument described here, the total [NO_2] signal in the ΣPNs channel can, however, be biased by a number of reactions initiated by the organic radicals. The influence of these reactions has been described in the literature (Day et al., 2002; Paul and Osthoff, 2010; Thieser et al., 2016). Taking the example of peroxyacetyl nitrate (PAN), subsequent to its thermal decomposition (Reaction R1a), there are processes that lead both to the removal of NO_2 (Reactions R1b, R5) and to its formation (Reactions R2, R3, R4).

$$CH_3C(O)O_2NO_2 + M \rightarrow CH_3C(O)O_2 + NO_2 + M \quad \text{(R1a)}$$

$$CH_3C(O)O_2 + NO_2 + M \rightarrow CH_3C(O)O_2NO_2 + M \quad \text{(R1b)}$$

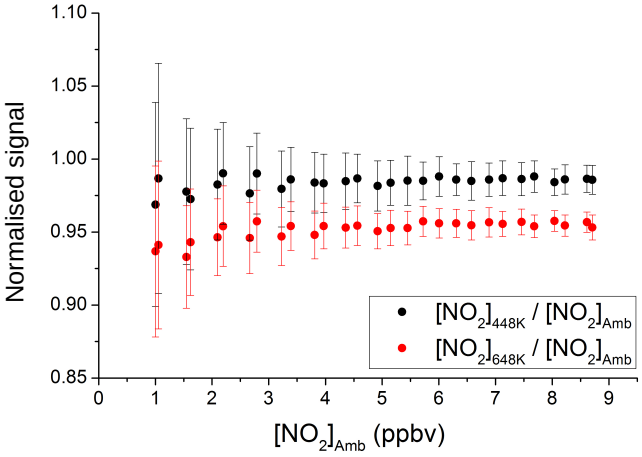

Figure 5. NO_2 loss in the heated inlets of the ΣPNs and ΣANs channels. Black points represent the NO_2 mixing ratio measured in the ΣPNs channel ($[NO_2]_{448\,K}$) normalised to the NO_2 mixing ratio measured in the NO_2 channel ($[NO_2]_{Amb}$). Red points represent the NO_2 mixing ratio measured in the ΣANs channel ($[NO_2]_{648\,K}$) normalised to the NO_2 signal measured in the NO_2 channel.

$$CH_3C(O)O_2 + NO(+O_2) \rightarrow NO_2 + CH_3O_2 + CO_2 \quad \text{(R2)}$$

$$CH_3O_2 + NO(+O_2) \rightarrow HCHO + HO_2 + NO_2 \quad \text{(R3)}$$

$$HO_2 + NO \rightarrow OH + NO_2 \quad \text{(R4)}$$

$$OH + NO_2 + M \rightarrow HNO_3 + M \quad \text{(R5)}$$

Reactions (R2)–(R4) show that, in the most unfavourable scenario, if all organic radicals react with NO, each peroxyacetyl radical can lead to the formation of three NO_2 molecules, biasing the result by the same factor. Likewise, the presence of very high NO_2 could conceivably result in complete reformation of PAN (Reaction R1b). The size and sign of the bias thus depends on the relative concentrations of NO and NO_2 and, most importantly, on the rate of loss of organic radicals to the reactor walls or via thermal decomposition. The bias resulting from these reactions can be reduced by minimising the residence time between thermal dissociation and detection and by making pressure-dependent recombination reactions inefficient by working at low pressures, e.g. by using LIF detection of NO_2 (Day et al., 2002; Wooldridge et al., 2010). As CRDS instruments operate at higher pressures, to maintain sufficient sensitivity (typically from 0.5 to 1 bar), we have taken a different approach and optimised the surface losses of the organic radicals by modifying the surface-to-volume ratio in the heated inlets.

First experiments on PAN samples using glass wool as a radical scavenger resulted in the desired reduction in the rate of recombination of $CH_3C(O)O_2$ with NO_2. Glass wool was, however, observed to greatly enhance (rather than reduce) the oxidation of NO to NO_2. This is presumably the result of a surface-catalysed process as previously observed on powdered, aluminium silicate mineral dust samples (Hanisch and Crowley, 2003), and may be related to the formation of ox-

idised surface sites that can react with NO. This led us to test glass beads, which presumably have less reactive "defective" sites than glass wool but a sufficient surface area to remove a large fraction of the organic radicals (see below). We conducted a series of experiments with different mixtures of PAN and NO_2 / NO (from 1 ppmv in synthetic air gas bottles) and analysis of the observations by numerical simulation, similar to that presented in Thieser et al. (2016).

The set of chemical reactions used in the numerical simulations is essentially the same as that described in Thieser et al. (2016). One exception is formation of NO_2 via the reaction between O_3 and NO, which Thieser et al. (2016) treated as occurring independently of other chemical processes. Here, this reaction is treated more rigorously by including it in the chemical simulation. The other difference is the use of two different values for a rate constant (k_s) used to calculate the kinetic limitation on the radical uptake coefficient (γ, see below). In order to simulate all laboratory data sets, different values of k_s (one for sections A and B and one for sections C and D; see Fig. S1 in Supplement) are required to account for the temperature gradient in the heated sections of the inlets. The heterogeneous loss of radicals to the reactor walls is based on a Langmuir–Hinshelwood mechanism, with the first-order rate constant (k_w) given by Eq. (2).

$$k_w = \frac{\gamma \bar{c} A}{4} \quad (2)$$

The uptake coefficient, γ, depends on both kinetic and diffusive limitations as described in detail by Thieser et al. (2016). Here we focus on the role of glass beads in enhancing the rate of uptake and reaction of organic radicals by increasing the surface area available for reaction (A). Without the glass beads, the value of A in the heated inlets is 3.5 $cm^2\,cm^{-3}$ (corresponding to a cylinder with internal diameter 1.2 cm). The presence of the glass beads, with an average diameter of 0.5 mm, results in a surface-to-volume ratio of $\approx 100\,cm^2\,cm^{-3}$. The exact determination of the temperature profile in the inlet is possible in the case of a classic cylindrical reactor, but is difficult to achieve with the presence of the glass beads and glass frit. An approximate profile in section D of the reactor (part of the cylindrical reactor between the fritted glass and the cavity inlet; see Fig. S1) was obtained by measuring the temperature between the fritted glass and the entrance of the cavity. It is assumed that the temperature in section B (containing the glass beads) increases from ambient to 448 K at the point where the gas enters section C (corresponding to the fritted glass section). This profile is also used to calculate the residence time in the ΣPNs channel of 1.3 s. To take into account the variations of temperature, pressure, specific surface area and diffusion radius along the glass reactor, a profile for each of these parameters is used as input in the numerical simulation.

Figure 6a shows results of a set of four experiments in which different amounts of PAN are mixed with different amounts of NO_2 and monitored in the three channels. The y axis shows the total [NO_2] measured in the ΣPNs channel ($[NO_2]_{448\,K}$) minus NO_2 measured in NO_2 channel ($[NO_2]_{Amb}$). The negative slopes of these data indicate that NO_2 from PAN decomposition is lost at high mixing ratios of added NO_2. A similar set of data, but with added NO rather than NO_2, is displayed in Fig. 6b. In this case, the positive slopes indicate that NO_2 is being formed from the reaction of organic radicals with NO. Note that the solid lines are the results of the numerical simulations (with identical mechanism) of NO_2 formation and loss in both experiments. The mixing ratios of PAN listed are those required in the model to match the experimental data. In both data sets the slopes are weakest at low PAN concentrations, reflecting the fact that radical-NO or radical-NO_2 reaction rates will be dependent on the radical concentrations. The mixing ratios of PAN cannot be derived by simple back extrapolation to zero NO_2 or NO as this does not take into account the NO_2 formed when PAN itself decomposes. At the highest mixing ratios of NO_2, up to 25 % of the peroxyacetyl radical recombines with NO_2 while the other 75 % is lost to the walls or did not react with NO_2.

The analysis of the measurements shows that (without correction) NO_2 would be overestimated by approximately 40 % for 3 ppb of PAN when sampling air containing 8 ppbv of NO. This is much lower that the ≈ 150 % reported by Thieser et al. (2016) for similar conditions in their ΣPNs channel, reflecting the increased loss of radicals on the glass surfaces.

In both series of experiments, the model reproduces the data for the whole range of [PAN], [NO_2] and [NO] explored. A set of experiments was carried out to investigate whether the formation (or loss) of NO_2 described above could be influenced by the presence of water vapour acting, for example, as a quencher of a surface reaction. A mixture of PAN plus NO_2 was humidified to 60 % RH, with other operating conditions similar to the previous experiments. The numerical model reproduced the measurement data without the need to modify the wall loss rates or add any chemical processes involving H_2O, suggesting that the gas and surface reactions taking place are not significantly influenced by adsorbed water at these temperatures. In order to correct field data for these biases, an iterative fitting procedure is used and described in detail in Sect. 4.2.

3.2.3 Reaction of radicals with NO / NO_2 in the ΣANs channel (648 K)

As first discussed by Thieser al. (2016), experimental and theoretical studies show that the higher temperature (648 K) of the ΣANs channel changes the chemical processes substantially compared to 448 K. ANs can now decompose to NO_2 and an alkyl radical fragment, whereas the peroxyacetyl radical (from PAN decomposition) is thermally unstable. The NO_2 generated in the ΣANs channel when adding NO_2 / NO to PAN samples is displayed in Fig. 6c and d. The results show a greatly reduced effect of NO_2 recombination or NO

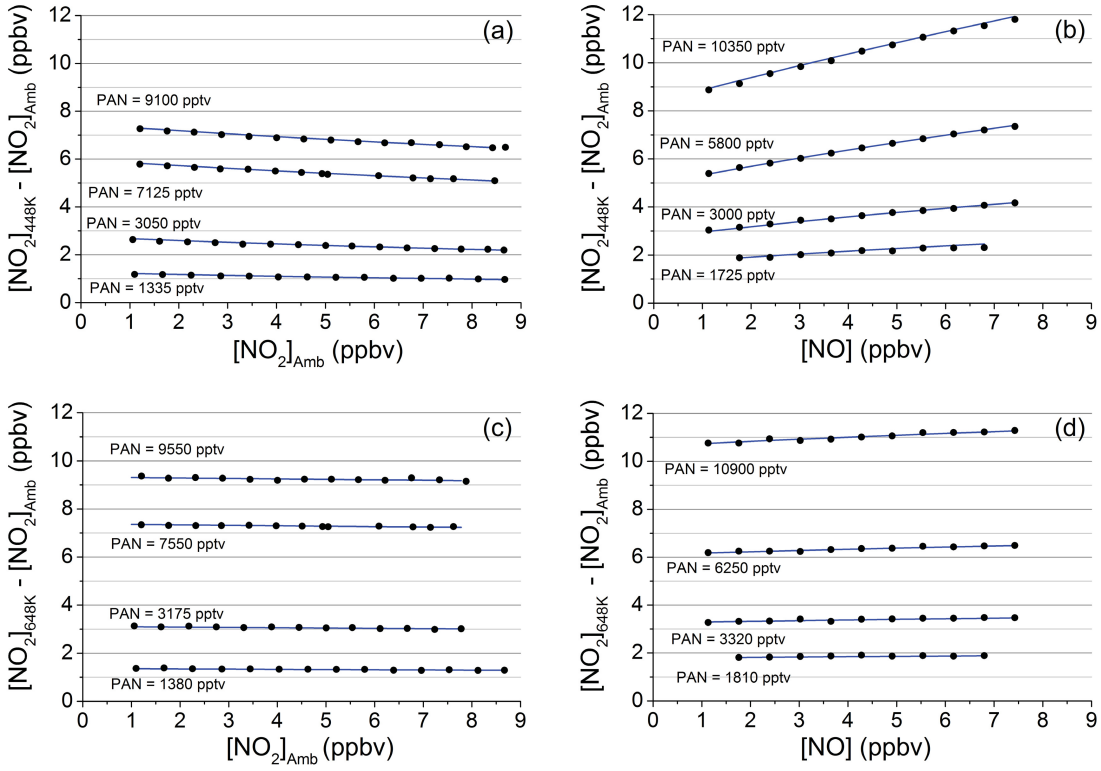

Figure 6. Modelled (lines) and measured difference between the NO_2 signal in the hot channels and ambient temperature channel for different PAN samples and different added amounts of NO and NO_2. **(a)** Addition of NO_2 to the 448 K (PNs) channel. **(b)** Addition of NO to the 448 K (PNs) channel. **(c)** Addition of NO_2 to the 648 K (ANs) channel. **(d)** Addition of NO_2 to the 648 K (ANs) channel.

oxidation compared to the ΣPNs channel (Fig. 6a, b), largely resulting from the instability of the of $CH_3C(O)O_2$ radical. The model takes into account two main pathways for the fate of the peroxyacetyl radical (Reactions R6, R7) in which the acetyl radical (CH_3CO) formed in Reaction (R6) can react further with O_2 to reform a peroxyacetyl radical or an OH radical and an α-lactone (Reactions R8, R9) (Carr et al., 2011). $CH_2C(O)OOH$ can also decompose to OH and an α-lactone (Reaction R10) (Carr et al., 2007, 2011; Chen and Lee, 2010). If not lost to the walls, OH can react with NO_2 to form HNO_3 according to Reaction (R5).

$$CH_3C(O)O_2 + M \rightarrow CH_3CO + O_2 + M \quad \text{(R6)}$$
$$CH_3C(O)O_2 \rightarrow CH_2C(O)OOH \quad \text{(R7)}$$
$$CH_3CO + O_2 + M \rightarrow CH_3C(O)O_2 + M \quad \text{(R8)}$$
$$CH_3CO + O_2 \rightarrow OH + C_2H_2O_2 \quad \text{(R9)}$$
$$CH_2C(O)OOH \rightarrow OH + C_2H_2O_2 \quad \text{(R10)}$$
$$CH_3CO + O_2 + M \rightarrow CH_3O_2 + CO + M \quad \text{(R11)}$$

The acetyl radical can also form a methylperoxy radical CH_3O_2 through the formation of a CH_3 radical and CO. The net reaction is given by Reaction (R11). In the presence of NO, the peroxy radicals ($CH_3C(O)O_2$, CH_3O_2 and HO_2), if not lost to the glass surface, can lead to the formation of NO_2.

To simulate the reactions in the ΣANs channel, the temperature profile was determined in the same way as the ΣPNs channel profile. Due to the higher gas flow velocity at the elevated temperatures, the pressure profile is slightly different than in the ΣPNs channel and gives a cavity pressure that is about 10 mbar lower. The results of the experiments involving addition of NO_2 to PAN samples in the ANs channel are presented in Fig. 6c. For the range of PAN concentrations covered, the loss of NO_2 by chemical recombination is about 5 % of the initial PAN. The initial PAN concentration used as input variable for the numerical simulations is, for all four experiments, about 3–5 % higher than that needed to fit the data obtained in the PNs channel (Fig. 6a), which is most probably related to model uncertainties. Since this 3–5 % difference is the same for all four experiments and is apparently not correlated with the amount of PAN, it is added to the calculation of total uncertainty for the PNs measurement. The results of the NO addition experiments are shown in Fig. 6d. The thermal decomposition of the peroxyacetyl radical reduces the positive bias due to NO oxidation so that a maximum factor of only 1.04 (compared to 1.40 in the ΣPNs channel) is obtained. The initial PAN concentration required to fit the NO addition data set at 648 K is 5–10 % higher than at 448 K, which is related to uncertainty in the [NO] mixing ratio used or a bias in the simulation.

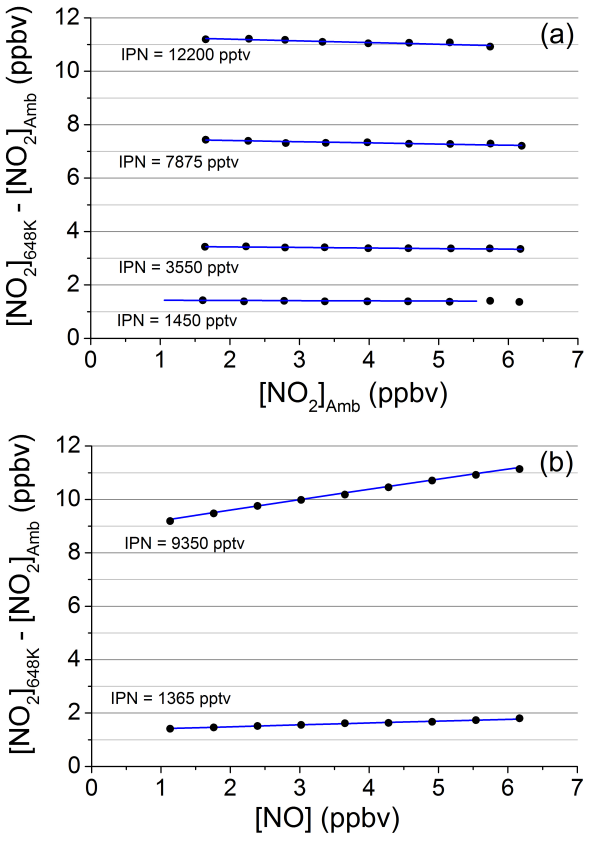

Figure 7. Modelled (lines) and measured difference between the NO_2 signal in the 648 K channels and ambient temperature channel for i-propyl nitrate (IPN) samples and different added amounts of NO_2 **(a)** or NO **(b)**.

In order to investigate the role of organic (alkyl) radicals generated from the thermal decomposition of ANs, a set of experiments was conducted in which a sample of i-propyl nitrate ($C_3H_7ONO_2$) in synthetic air was mixed with different amounts of NO and NO_2. Thermal decomposition of i-propyl nitrate (Reaction R12) is followed by Reactions (R13) and (R14) that generate HO_2 and CH_3O_2, which can convert NO to NO_2 and sequester NO_2 as HO_2NO_2 and $CH_3O_2NO_2$.

$$C_3H_7ONO_2 \rightarrow C_3H_7O + NO_2 \quad \text{(R12)}$$
$$C_3H_7O + O_2 \rightarrow CH_3C(O)CH_3 + HO_2 \quad \text{(R13)}$$
$$C_3H_7O + M \rightarrow CH_3 + CH_3CHO + M \quad \text{(R14)}$$

Figure 7a and b show that the addition of NO increases the amount of NO_2 formed per AN, whereas the presence of NO_2 results in a negative bias to the data. These effects are captured well for both data sets by the model simulations (blue lines).

3.2.4 Effect of thermal decomposition of O_3

At high temperatures, O_3 decomposes according to Reaction (R15). Although most of the O atom produced reacts with O_2 to reform ozone (Reaction R16), it can form NO+O_2 in the presence of NO_2 (Reaction R17).

$$O_3 \rightarrow O_2 + O \quad \text{(R15)}$$
$$O + O_2 + M \rightarrow O_3 + M \quad \text{(R16)}$$
$$O + NO_2 \rightarrow O_2 + NO \quad \text{(R17)}$$

The importance of this process is strongly dependent on the operating conditions of the instrument, recent studies showing that higher temperatures or pressures may result in a significant, negative bias from the ozone-pyrolysis-initiated reduction of NO_2 (Lee et al., 2014; Thieser et al., 2016). Assuming that the steady-state concentration of the O atom in the heated inlets is dominated by Reactions (R15) and (R16) ($k_{16}[O_2] \gg k_{17}[NO_2]$), the loss of NO_2 can be approximated as follows:

$$-d[NO_2] = [NO_2][O_3]\left(\frac{k_{15}k_{17}}{k_{16}[O_2]}t\right). \quad (3)$$

The term in brackets is constant at constant temperature, pressure and flow rate through the heated inlet, and can be determined experimentally by sampling different mixtures of NO_2 and O_3 simultaneously through the ambient temperature channel and the two hot channels. Figure 8 shows the difference $[NO_2]_{Amb} - [NO_2]_{648\,K}$ (in ppbv) as a function of $[NO_2] \times [O_3]$ for three different levels of ozone (50, 115 and 185 ppbv). A linear fit through the data points yields a slope of $2.54 \pm 0.26 \times 10^{-4}$ ppbv^{-1}, which is $< 50\,\%$ of the value found by Thieser et al. (2016). The difference can be attributed mainly to the use of a lower oven temperature (648 K in this work instead of 723 K). No reduction of NO_2 is observed in the ΣPNs channel because thermal decomposition of O_3 at 448 K is too slow. To illustrate the impact of the thermal dissociation of O_3 in the ANs channel, we note

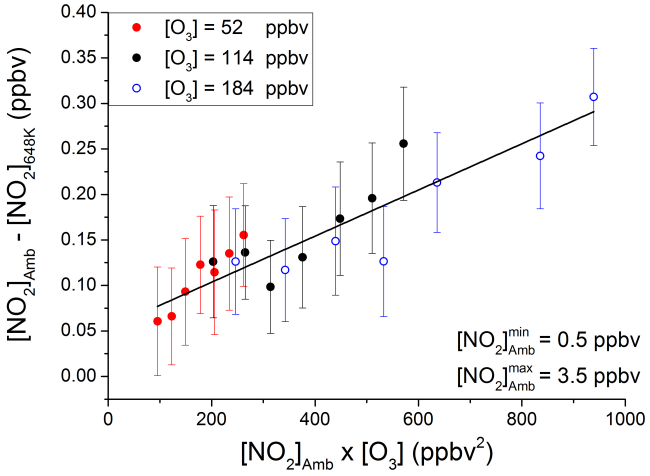

Figure 8. Influence of O_3 pyrolysis. Loss of NO_2 (in ppbv) in the heated ΣANs channel compared to the NO_2 channel vs. the product of the NO_2 and O_3 mixing ratios.

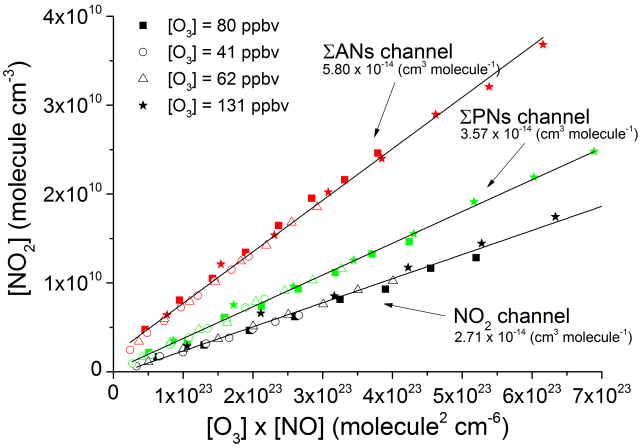

Figure 9. Production of NO_2 from the $O_3 + NO$ reaction when sampling into the three 405 nm channels with different amounts of NO and O_3. The numbers in parentheses are the slopes of least-squares fits (solid lines), which correspond to the product of the effective second-order rate constant and the reaction time.

that 5 ppbv of total NO_2 in the presence of 50 ppbv of O_3 results in the removal of 75 pptv NO_2. Since the amount of O_3 decomposed and NO produced in this process is negligible compared to ambient amounts, it does not affect the input conditions for the numerical simulations, and can therefore be treated separately using Eq. (3).

3.2.5 Effect of NO oxidation by O_3

A positive bias to the measurement of NO_2 may result from NO oxidation by O_3 during the time it takes for the sampled air to flow through the inlets and cavities of the instrument (Reaction R18).

$$NO + O_3 \rightarrow NO_2 \qquad \text{(R18)}$$

The rate coefficient of this reaction is temperature-dependent, and the effect is larger at 448 and 648 K than at room temperature. To investigate this interference, different mixtures of O_3 and NO were sampled simultaneously through the three channels. The results are shown in Fig. 9 where data from four experiments with different O_3 mixing ratios (41, 62, 80 and 131 ppbv) are plotted. The solid lines are fits to the data, the slopes of which are second-order rate constants multiplied by a reaction time ($cm^3\,molecule^{-1}$). The rate constant for the gas-phase reaction between NO and O_3 is listed as $k_{O_3+NO} = 9 \times 10^{-19} \exp(-850/T) \times T^{2.25}\,cm^3\,molecule^{-1}\,s^{-1}$ (Atkinson et al., 2004). For the ΣPNs channel (448 K), using this expression results in an underestimation of the effective (measured) production of NO_2 by a factor 1.06. For the ΣANs (648 K) channel the equivalent factor is 1.52. The most likely reason for this discrepancy is that some NO is oxidised in a surface catalysed process, presumably involving surface sites that are activated following interaction with O_3. To account for this extra source of NO_2, the O_3 plus NO reaction is implemented in the chemical model (with modified rate expressions) for the 448 and 648 K data corrections (see Sect. 3.2.2 and 3.2.3), and corrected manually for the NO_2 channel.

3.2.6 Detection of other species as NO_2 after thermal dissociation

Atmospheric trace gases other than PNs and ANs can potentially be detected as NO_2 in this instrument. As thermal decomposition of N_2O_5 to NO_3 and NO_2 has been shown to be 100 % efficient in our 383 K inlet in the 662 nm channels, we expect 100 % dissociation at the higher temperatures of the ΣPNs and ΣANs channels. This may represent a significant source of bias during the night when N_2O_5 mixing ratios can be large. However, as the five-channel instrument simultaneously monitors N_2O_5, this can be easily corrected. Here we consider possible HNO_3 and $ClNO_2$ interferences in the ΣANs channel.

HNO_3 is a major reservoir of tropospheric NO_x. Although HNO_3 is thermally stable at temperatures below 700 K, Wild et al. (2014) report ≈ 95 % conversion of HNO_3 to NO_2 at 648 K, whereas Thieser et al. (2016) found about 10 % at 723 K. In order to test for unwanted detection of HNO_3 when sampling from the hot inlets (with glass beads) in the five-channel instrument, we injected a sample of HNO_3 in synthetic air directly prior to the flow division before entering the three 405 nm channels. In this way, possible losses of HNO_3 in the inlet in front of the heated sections of the instrument were minimised. HNO_3 was generated in a custom-built permeation source, which was calibrated by absorption spectroscopy at 184.85 nm, where HNO_3 absorbs strongly. The permeation source generated several ppmv of HNO_3 in a flow of 10 sccm, which, following dilution, provided a mixing ratio of ≈ 30 ppbv at the CRDS inlet. The permeation source also generated about 3 ppbv of NO_2. Figure 4 (open circles) shows that NO_2 arising from HNO_3 decomposition could not be observed in either heated inlet, enabling us to set an upper limit to the decomposition efficiency of HNO_3 to NO_2 of < 0.5 %. This is in broad agreement with the previous measurement by Thieser et al. (2016), who saw no evidence for HNO_3 decomposition below 650 K, and is in stark contrast to that reported by Wild et al. (2014). While we have no rigorous explanation of this, we note that the gas-phase thermal dissociation of HNO_3 to NO_2 at the temperature of these experiments is too slow to explain its formation, which suggests that it is probably surface-catalysed in the experiments of Wild et al. (2014), implying that different glass types or chemical history of the surface may influence the formation of NO_2 significantly.

As reported previously, $ClNO_2$, formed in the atmosphere in the reaction between N_2O_5 and chloride-containing particles, can be detected as NO_2 in TD-CRDS instruments (Thaler et al., 2011; Wild et al., 2014; Thieser et al., 2016) The $ClNO_2$ decomposition efficiency as a function of the

oven temperature is plotted in Fig. 4. The $ClNO_2$ sample was generated by flowing Cl_2 in synthetic air over sodium nitrite crystals. In normal operating conditions (at 648 K), 90 ± 3 % of the $ClNO_2$ is decomposed to NO_2. As $ClNO_2$ mixing ratios are highly variable and can approach ppbv levels, $ClNO_2$ may thus represent a serious limitation to ANs measurements, unless independent measurements are available to enable correction.

3.2.7 Detection limit and total uncertainty for NO_2, PNs and ANs

The detection limit for the 405 nm channels can be estimated in a similar manner to that described for the 662 nm channels. The 2σ standard deviation for consecutive zeros for the NO_2, ΣPNs and ΣANs channels are respectively 59, 74 and 54 pptv. Using these values, we obtain detection limits for [NO_2], [PNs] and [ANs] of 59, 94 and 80 pptv. The detection limits for [PNs] and [ANs] are obtained by error propagation on the NO_2 and PNs channels and NO_2 and ANs channel (see Sect. 4).

The total uncertainty associated with the [NO_2] measurement is a combination of the uncertainties in the l-to-d ratio, humidity matching of the zero and ambient air and the correction for the $NO + O_3$ reaction on the absorption cross section of NO_2 and on N_2O_5 decomposition. The total uncertainty on the absorption cross section is estimated to 6 %, taking into account the error on the reference cross section (Voigt et al., 2002) and fluctuation in the laser emission spectrum. This value, when combined with the uncertainty associated with the l-to-d ratio, results in 6.5 % uncertainty. The uncertainty associated with the correction for NO_2 formation in the $NO + O_3$ reaction depends on ambient ozone and NO levels. Considering 10 % uncertainty for k_{O_3+NO} and 5 % uncertainty for [O_3], [NO] and [NO_2], [NO] and [O_3] ambient levels of 1, 0.5 and 50 ppbv, we obtain an uncertainty for this correction of 0.1 % on the final [NO_2] value. NO_2 can be formed at room temperature by the slow thermal decomposition of N_2O_5. Taking a decomposition rate constant of 4.4×10^{-2} s^{-1} at 303 K for N_2O_5 (Atkinson et al., 2016) and a residence time in the NO_2 channel of 1.7 s, we calculate that 0.08 of the N_2O_5 can decompose. The largest N_2O_5-to-NO ratio measured during NOTOMO was 0.17, which results in a maximum contribution of ≈ 1.5 % NO_2 from N_2O_5 decomposition. As mentioned in Sect. 2.2, the upper limit for bias caused by humidity matching errors when zeroing is 10 pptv, which results in a final uncertainty for [NO_2] of 8 % + 10 pptv.

The uncertainty of the total NO_2 detected in the ΣPNs and ΣANs channels is a combination of the same uncertainties involved in the [NO_2] measurement plus the uncertainty of the NO_2 transmission through the heated glass beads. Taking the values listed in Sect. 3.2.1, we obtain an uncertainty for total NO_2 detected of 7 % pptv for both ΣPNs and ΣANs channels. To correct for the radical plus NO_x biases, the total NO_2 signals measured in the two hot channels are used to constrain the chemical model described earlier. The uncertainty arising from these calculations depends on the total [NO_2] measured in each channel, and is thus highly variable. Note that uncertainty arising from the humidity difference is cancelled out by the subtraction to obtain [PNs] and [ANs]. The uncertainty added by the calculation of the ambient [PNs] and [ANs] depends on the model uncertainties, as well as on the uncertainty associated with the trace gas concentrations involved in this calculation. The uncertainty associated with [ΣPNs] and [ΣANs] is related to ambient [NO_2], [O_3] and [NO]. The fact that the corrections rely on PAN and IPN chemistry led Thieser et al. (2016) to estimate the uncertainty associated with the model-derived corrections to be 30 % (max) of the overall correction factor. The final uncertainties on the [ΣPNs] and [ΣANs] value depend on the total NO_2 signal in all three channels, and can vary significantly. Below, we discuss the correction factors required for the NO_2, ΣPNs and ΣANs data sets obtained during the first field deployment of the instrument.

4 First field deployment of the five-channel CRDS

The instrument described here was first deployed during the NOTOMO campaign (Nocturnal Observations at the Taunus Observatory; insights into Mechanisms of Oxidation) that took place during summer 2015. The site, previously described in detail (Crowley et al., 2010; Sobanski et al., 2016), is situated on top of the Kleiner Feldberg mountain (≈ 850 m a.s.l.) at the southern limit of the forested Taunus mountain range and north of the Frankfurt–Mainz–Wiesbaden agglomeration. The set of instruments deployed during NOTOMO was located in two research containers, and sampled from a common inlet. Approximately ≈ 10 m^3 min^{-1} air was drawn from a height of 8 m above ground through a 15 cm diameter stainless-steel pipe connected to an industrial fan. Gases were sampled (≈ 23 slm) in the TD-CRDS (located in the upper container) from the centre of the high-flow inlet via 1/2 in. PFA tubing (for the two 662 nm channels) and 1/3 in. PFA tubing (for the three 405 nm channels) ≈ 3.5 m from the top of the inlet. Residence times in the high flow inlet, in the 1/2 in. PFA tubing and in the 1/4 in. PFA tubing were 0.3, 0.05 and 0.1 s, respectively. In the following sections we shall not attempt to perform a detailed analysis of the entire campaign data set, which is beyond the scope of this paper, but provide a more qualitative description of the results, and indicate the size of corrections applied and the total uncertainty.

4.1 Mixing ratios of NO_2, NO_3, N_2O_5

Figure 10a shows the measured mixing ratios of NO_2, NO_3, N_2O_5, ΣPNs and ΣANs for 1 week between 30 June and 7 July. During this period, [NO_2] varied from 0.3 to 6 ppbv,

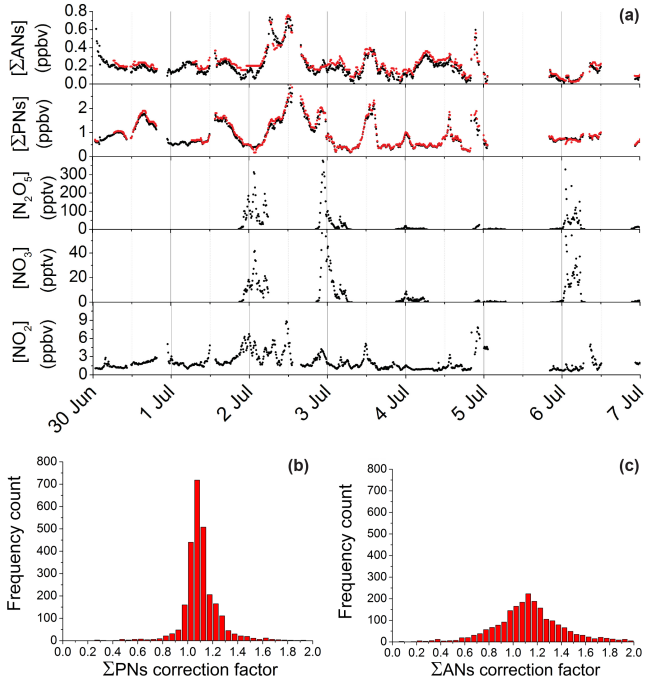

Figure 10. **(a)** Mixing ratios of NO_2, NO_3, N_2O_5, ΣPNs and ΣANs measured by the TD-CRDS instrument between 30 June and 7 July 2015 at the Kleiner Feldberg observatory, Germany, as part of the NOTOMO campaign. For the three lowest panels in ([NO_2], [NO_3] and [N_2O_5], the black points represent the final corrected data. For the ΣPNs panel, the black points correspond to uncorrected data obtained by subtracting [NO_2] measured in the NO_2 channel from the NO_2 measured in the ΣPNs channel. The red points have been corrected using the chemical model with the iterative fitting procedure. For the ΣANs panel, the black points correspond to the uncorrected data (obtained by subtracting the NO_2 signal measured in the ΣPNs channel from the NO_2 signal measured in the ΣANs channel). The red points have been corrected using the chemical model plus iterative fitting procedure. Panels **(b)** and **(c)** are frequency distributions for the correction factors applied using the iterative numerical simulations.

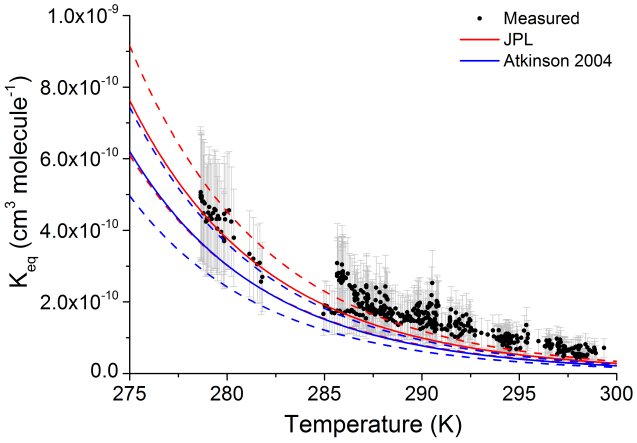

Figure 11. Equilibrium constant (K_{eq}) for the reaction $NO_2 + NO_3 = N_2O_5$ calculated from measurement of each trace gas (black points, with grey bars representing total uncertainty). The solid lines are values of K_{eq} recommended by the JPL evaluation panel (red line; Burkholder et al., 2016) and IUPAC evaluation committee (blue line; Atkinson et al., 2004). The dashed lines represent the minimum and maximum values according to the evaluations.

with an average value of 1.8 ppbv. NO_3 and N_2O_5 mixing ratios reach up to 40 and 400 pptv at night, and are below the detection limit during the day. These values are in the range of previous measurements at this location (Crowley et al., 2010; Sobanski et al., 2016), in which NO_2, NO_3 and N_2O_5 mixing ratios of up to 20, ≈200 and ≈3000 pptv, respectively were measured. Within a few minutes after sunset, NO_2, NO_3 and N_2O_5 acquire thermal equilibrium and the equilibrium constant, K_{eq}, can be calculated from [N_2O_5] / [NO_2][NO_3]. In Fig. 11 we compare temperature-dependent values of the equilibrium constant using measured concentrations of NO_2, NO_3 and N_2O_5 as well as values from the literature that are based on laboratory measurements (Atkinson et al., 2004; Burkholder et al., 2016). Within combined uncertainty, the values agree, though we note that the parameterisation of Burkholder et al. (2016) results in values that are closer to those obtained by analysing the field measurements and that the agreement is better at lower temperatures. We are wary of over-interpretation of this fact and are aware that the laboratory determinations that led to the recommended values are expected to be more accurate, especially close to room temperature where many data sets exist and are in good agreement. In this context we note that small errors in the measurement of the ambient temperature or a 10–20 % inlet loss of NO_3 would have been difficult to observe but would have had a significant impact on the equilibrium constant calculated from the field data and may have contributed to the differences observed.

4.2 Mixing ratios of ΣPNs and ΣANs

By simply subtracting [NO_2] measured by the NO_2 channel from the total NO_2 signal measured by the PAN channel and the total NO_2 signal in the ΣPNs channel from the total NO_2 signal in ΣANs channel, we obtain uncorrected mixing ratios for ΣPNs and ΣANs, which are plotted (black data points) in Fig. 10. In this context, uncorrected means that no chemical corrections have been applied (e.g. for reformation of PNs in the presence of NO_2, or formation of NO_2 from NO oxidation with O_3 see Sect. 3) but physical corrections (e.g. *l*-to-*d* ratio) have been made.

The procedure used to correct the [ΣPNs] and [ΣANs] mixing ratios for the effects described in Sect. 3 utilises an iterative algorithm based on the chemical model used to simulate the laboratory data described in Sect. 3.2. To correct the ΣPNs data, a simulation using [NO_2], [O_3] and [NO] values and an initial guess for [ΣPNs] were performed. Values

of O_3 were taken from ambient measurements, whereas, in the absence of NO measurements, we assumed that its mixing ratio was zero at night-time and during the day could be calculated from its photochemical steady state, $[NO]_{ss} = J_{NO_2}[NO_2]/k_{NO+O_3}\ [O_3]$, where J_{NO_2} is the photolysis frequency of NO_2 (measured using a spectral radiometer) and k_{NO+O_3} is the rate constant for reaction of NO with O_3. This method of estimating [NO] resulted in satisfactory agreement with measurements from the Hessian Agency for Nature Conservation, Environment and Geology (HLUG) for periods when NO was above the detection limit (> 1 ppb) of their instrument, which monitors NO permanently at the site.

In the iterative procedure, [ΣPNs] were tuned automatically until the simulated total $[NO_2]$ matched the measured $[NO_2]$ in the ΣPNs channel. This procedure was applied to each data point (10 min resolution) obtained during the campaign. The corrected [ΣPNs] were used as an additional input to correct the [ΣANs] data. In this case, constant values for $[NO_2]$, $[O_3]$, $[NO_2]$ and [ΣPNs] and a variable value for [ΣANs] are inputted into the model to match the total NO_2 signal measured in the ΣANs channel. For the correction of the [ΣPNs] data, ambient N_2O_5 was taken into account by adding its mixing ratio to the initial $[NO_2]$ values. This was also done also for the [ΣANs] correction. Measured $ClNO_2$ mixing ratio was decreased by a factor of 0.9 to account for the decomposition efficiency and was then added to the initial $[NO_2]$ for simulation of the total NO_2 in the ΣANs channel. The corrected data are displayed as red data points in Fig. 10a.

The overall correction factor (corrected data/uncorrected data) required for the ΣPNs and ΣANs measurements are illustrated in Fig. 10b and c. The peak of the distributions is at ≈ 1.1 for both data sets, and the sigma values corresponding to a Gaussian fit are 0.06 and 0.18 for ΣPNs and ΣANs respectively, indicating that the corrections required are dominated by NO_2 rather than NO, and that the corrections for the ΣANs vary more due to the presence of more organic radicals in the ΣANs channel.

5 Conclusions

We have constructed and characterised a five-channel, thermal-dissociation cavity ring-down spectrometer for measurement of the reactive nitrogen traces gases, NO_2, NO_3, N_2O_5 peroxy nitrates and alkyl nitrates, which provides insight into the coupling of atmospheric, daytime and night-time NO_x and RO_x chemistry. The total measurement uncertainties and limits of detection are estimated at 25 % and 2 pptv for NO_3, 28 % and 10 pptv for N_2O_5 and 6.5 % +10 and 59 pptv for NO_2.

Chemical interferences in the measurements of PNs and ANs were reduced by the use of low TD temperatures and the use of glass beads as the radical scavenger. In combination with extensive laboratory tests to enable accurate correction for bias in PNs and ANs measurements resulting from reactions of organic radicals formed in the thermal-dissociation channels, this reduces overall uncertainty and extends the NO_x regime in which the instrument can be operated. The total uncertainty associated with the PNs and ANs measurements is dependent on NO_x levels and also on the presence (mainly at night) of $ClNO_2$ and N_2O_5. During the PARADE campaign the average correction was (1.1 ± 0.3) where the quoted uncertainty is an estimate of systematic error related to the use of a numerical model to simulate chemical processes in the TD sections of the instrument.

6 Data availability

The PARADE data can be obtained on request (via John Crowley) from the owners. The NOTOMO data will be released at the end of 2017.

The Supplement related to this article is available online at doi:10.5194/amt-9-5103-2016-supplement.

Acknowledgements. We are grateful to the following: Bernard Brickwedde for technical/software assistance. We thank DuPont for provision of a sample of the FEP used to coat the cavity walls. We thank Heinz Bingemer for logistical support and use of the facilities at the Taunus Observatory during the NOTOMO campaign. This work was carried out in part fulfilment of the PhD of Nicolas Sobanski at the Johannes Gutenberg University in Mainz, Germany.

The article processing charges for this open-access publication were covered by the Max Planck Society.

Edited by: D. Toohey
Reviewed by: two anonymous referees

References

Allan, B. J., Carslaw, N., Coe, H., Burgess, R. A., and Plane, J. M. C.: Observations of the nitrate radical in the marine boundary layer, J. Atmos. Chem., 33, 129–154, 1999.

Arey, J., Aschmann, S. M., Kwok, E. S. C., and Atkinson, R.: Alkyl Nitrate, Hydroxyalkyl Nitrate, and Hydroxycarbonyl Formation from the NO_x Air Photooxidations of C_5-C_8 n-Alkanes, J. Phys. Chem. A, 105, 1020–1027, 2001.

Atkinson, R., Baulch, D. L., Cox, R. A., Crowley, J. N., Hampson, R. F., Hynes, R. G., Jenkin, M. E., Rossi, M. J., and Troe, J.: Evaluated kinetic and photochemical data for atmospheric chemistry: Volume I – gas phase reactions of O_x, HO_x, NO_x and SO_x species, Atmos. Chem. Phys., 4, 1461–1738, doi:10.5194/acp-4-1461-2004, 2004.

Beaver, M. R., Clair, J. M. St., Paulot, F., Spencer, K. M., Crounse, J. D., LaFranchi, B. W., Min, K. E., Pusede, S. E., Wooldridge,

P. J., Schade, G. W., Park, C., Cohen, R. C., and Wennberg, P. O.: Importance of biogenic precursors to the budget of organic nitrates: observations of multifunctional organic nitrates by CIMS and TD-LIF during BEARPEX 2009, Atmos. Chem. Phys., 12, 5773–5785, doi:10.5194/acp-12-5773-2012, 2012.

Berden, G., Peeters, R., and Meijer, G.: Cavity ring-down spectroscopy: Experimental schemes and applications, Int. Rev. Phys. Chem., 19, 565–607, 2000.

Blanchard, P., Shepson, P. B., Schiff, H. I., and Drummond, J. W.: Development of a gas chromatograph for trace gas-chromatograph for trace-level measurement of peroxyacetyl nitrate using chemical amplification, Anal. Chem., 65, 2472–2477, doi:10.1021/ac00066a012, 1993.

Brown, S. S.: Absorption spectroscopy in high-finesse cavities for atmospheric studies, Chem. Rev., 103, 5219–5238, 2003.

Burkholder, J. B., Sander, S. P., Abbatt, J., Barker, J. R., Huie, R. E., Kolb, C. E., Kurylo, M. J., Orkin, V. L., Wilmouth, D. M., and Wine, P. H.: Chemical Kinetics and Photochemical Data for Use in Atmospheric Studies, Jet Propulsion Laboratory, Pasadena, Evaluation No. 18, JPL Publication 15-10, available at: http://jpldataeval.jpl.nasa.gov., 2016.

Carr, S. A., Baeza-Romero, M. T., Blitz, M. A., Pilling, M. J., Heard, D. E., and Seakins, P. W.: OH yields from the $CH_3CO + O_2$ reaction using an internal standard, Chem. Phys. Lett., 445, 108–112, 2007.

Carr, S. A., Glowacki, D. R., Liang, C.-H., Baeza-Romero, M. T., Blitz, M. A., Pilling, M. J., and Seakins, P. W.: Experimental and modeling studies of the pressure and temperature dependences of the kinetics and the OH yields in the acetyl $+ O_2$ reaction, J. Phys. Chem. A, 115, 1069–1085, 2011.

Chen, S.-Y. and Lee, Y.-P.: Transient infrared absorption of t-$CH_3C(O)OO$, c-$CH_3C(O)OO$, and α-lactone recorded in gaseous reactions of CH_3CO and O_2, J. Chem. Phys., 132, 114303, doi:10.1063/1.3352315, 2010.

Crowley, J. N., Schuster, G., Pouvesle, N., Parchatka, U., Fischer, H., Bonn, B., Bingemer, H., and Lelieveld, J.: Nocturnal nitrogen oxides at a rural mountain-site in south-western Germany, Atmos. Chem. Phys., 10, 2795–2812, doi:10.5194/acp-10-2795-2010, 2010.

Day, D. A., Wooldridge, P. J., Dillon, M. B., Thornton, J. A., and Cohen, R. C.: A thermal dissociation laser-induced fluorescence instrument for in situ detection of NO_2, peroxy nitrates, alkyl nitrates, and HNO_3, J. Geophys. Res., 107, ACH 4-1–ACH 4-14, doi:10.1029/2001jd000779, 2002.

Day, D. A., Dillon, M. B., Wooldridge, P. J., Thornton, J. A., Rosen, R. S., Wood, E. C., and Cohen, R. C.: On alkyl nitrates, O_3, and the "missing NO_y", J. Geophys. Res., 108, 4501, doi:10.1029/2003jd003685, 2003.

Dorn, H.-P., Apodaca, R. L., Ball, S. M., Brauers, T., Brown, S. S., Crowley, J. N., Dubé, W. P., Fuchs, H., Häseler, R., Heitmann, U., Jones, R. L., Kiendler-Scharr, A., Labazan, I., Langridge, J. M., Meinen, J., Mentel, T. F., Platt, U., Pöhler, D., Rohrer, F., Ruth, A. A., Schlosser, E., Schuster, G., Shillings, A. J. L., Simpson, W. R., Thieser, J., Tillmann, R., Varma, R., Venables, D. S., and Wahner, A.: Intercomparison of NO_3 radical detection instruments in the atmosphere simulation chamber SAPHIR, Atmos. Meas. Tech., 6, 1111–1140, doi:10.5194/amt-6-1111-2013, 2013.

Everest, M. A. and Atkinson, D. B.: Discrete sums for the rapid determination of exponential decay constants, Rev. Sci. Instrum., 79, 023108, doi:10.1063/1.2839918, 2008.

Flocke, F., Volz-Thomas, A., and Kley, D.: Measurements of alkyl nitrates in rural and polluted air masses, Atmos. Environ. A-Gen., 25, 1951–1960, 1991.

Fuchs, H., Dube, W. P., Lerner, B. M., Wagner, N. L., Williams, E. J., and Brown, S. S.: A Sensitive and Versatile Detector for Atmospheric NO_2 and NO_x Based on Blue Diode Laser Cavity Ring-Down Spectroscopy, Environ. Sci. Technol., 43, 7831–7836, doi:10.1021/es902067h, 2009.

Fuchs, H., Ball, S. M., Bohn, B., Brauers, T., Cohen, R. C., Dorn, H.-P., Dubé, W. P., Fry, J. L., Häseler, R., Heitmann, U., Jones, R. L., Kleffmann, J., Mentel, T. F., Müsgen, P., Rohrer, F., Rollins, A. W., Ruth, A. A., Kiendler-Scharr, A., Schlosser, E., Shillings, A. J. L., Tillmann, R., Varma, R. M., Venables, D. S., Villena Tapia, G., Wahner, A., Wegener, R., Wooldridge, P. J., and Brown, S. S.: Intercomparison of measurements of NO_2 concentrations in the atmosphere simulation chamber SAPHIR during the NO3Comp campaign, Atmos. Meas. Tech., 3, 21–37, doi:10.5194/amt-3-21-2010, 2010.

Fuchs, H., Simpson, W. R., Apodaca, R. L., Brauers, T., Cohen, R. C., Crowley, J. N., Dorn, H.-P., Dubé, W. P., Fry, J. L., Häseler, R., Kajii, Y., Kiendler-Scharr, A., Labazan, I., Matsumoto, J., Mentel, T. F., Nakashima, Y., Rohrer, F., Rollins, A. W., Schuster, G., Tillmann, R., Wahner, A., Wooldridge, P. J., and Brown, S. S.: Comparison of N_2O_5 mixing ratios during NO3Comp 2007 in SAPHIR, Atmos. Meas. Tech., 5, 2763–2777, doi:10.5194/amt-5-2763-2012, 2012.

Hanisch, F. and Crowley, J. N.: heterogeneous reactivity of NO and HNO_3 on mineral dust in the presence of ozone, Phys. Chem. Chem. Phys., 5, 883–887, 2003.

Johnston, H. S., Davis, H. F., and Lee, Y. T.: NO_3 photolysis product channels: Quantum yields from observed energy thresholds, J. Phys. Chem., 100, 4713–4723, doi:10.1021/jp952692x, 1996.

Kirchner, F., Mayer-Figge, A., Zabel, F., and Becker, K. H.: Thermal stability of peroxynitrates, Int. J. Chem. Kinet., 31, 127–144, 1999.

Lee, L., Wooldridge, P. J., Gilman, J. B., Warneke, C., de Gouw, J., and Cohen, R. C.: Low temperatures enhance organic nitrate formation: evidence from observations in the 2012 Uintah Basin Winter Ozone Study, Atmos. Chem. Phys., 14, 12441–12454, doi:10.5194/acp-14-12441-2014, 2014.

Lehmann, K. K. and Romanini, D.: The superposition principle and cavity ring-down spectroscopy, J. Chem. Phys., 105, 10263–10277, doi:10.1063/1.472955, 1996.

Murphy, J. G., Thornton, J. A., Wooldridge, P. J., Day, D. A., Rosen, R. S., Cantrell, C., Shetter, R. E., Lefer, B., and Cohen, R. C.: Measurements of the sum of HO_2NO_2 and $CH_3O_2NO_2$ in the remote troposphere, Atmos. Chem. Phys., 4, 377–384, doi:10.5194/acp-4-377-2004, 2004.

O'Keefe, A. and Deacon, D. A. G.: Cavity ring-down optical spectrometer for absorption measurements using pulsed laser sources, Rev. Sci. Instrum., 59, 2544–2551, doi:10.1063/1.1139895, 1988.

Orphal, J., Fellows, C. E., and Flaud, P. M.: The visible absorption spectrum of NO_3 measured by high-resolution Fourier transform spectroscopy, J. Geophys. Res., 108, 4077, doi:10.1029/2002JD002489, 2003.

Osthoff, H. D., Pilling, M. J., Ravishankara, A. R., and Brown, S S.: Temperature dependence of the NO_3 absorption cross-section above 298 K and determination of the equilibrium constant for $NO_3 + NO_2 <-> N_2O_5$ at atmospherically relevant conditions, Phys. Chem. Chem. Phys., 9, 5785–5793, 2007.

Paul, D. and Osthoff, H. D.: Absolute Measurements of Total Peroxy Nitrate Mixing Ratios by Thermal Dissociation Blue Diode Laser Cavity Ring-Down Spectroscopy, Anal. Chem., 82, 6695–6703, doi:10.1021/ac101441z, 2010.

Paul, D., Furgeson, A., and Osthoff, H. D.: Measurements of total peroxy and alkyl nitrate abundances in laboratory-generated gas samples by thermal dissociation cavity ring-down spectroscopy, Rev. Sci. Instrum., 80, 114101, doi:10.1063/1.3258204, 2009.

Perring, A. E., Pusede, S. E., and Cohen, R. C.: An observational perspective on the atmospheric impacts of alkyl and multifunctional nitrates on ozone and secondary organic aerosol, Chem. Rev., 113, 5848–5870, doi:10.1021/cr300520x, 2013.

Platt, U., Perner, D., Winer, A. M., Harris, G. W., and Pitts, J. N. J.: Detection of NO_3 in the polluted troposphere by differential optical absorption, Geophys. Res. Lett., 7, 89–92, doi:10.1029/GL007i001p00089, 1980.

Roberts, J. M.: The atmospheric chemistry of organic nitrates, Atmos. Environ. A-Gen., 24, 243–287, doi:10.1016/0960-1686(90)90108-y, 1990.

Roberts, J. M., Fajer, R. W., and Springston, S. R.: Capillary gas-chromatographic separation of alkyl nitrates and peroxycarboxylic nitric anhydrides, Anal. Chem., 61, 771–772, doi:10.1021/ac00182a026, 1989.

Schuster, G., Labazan, I., and Crowley, J. N.: A cavity ring down/cavity enhanced absorption device for measurement of ambient NO_3 and N_2O_5, Atmos. Meas. Tech., 2, 1–13, doi:10.5194/amt-2-1-2009, 2009.

Slusher, D. L., Huey, L. G., Tanner, D. J., Chen, G., Davis, D. D., Buhr, M., Nowak, J. B., Eisele, F. L., Kosciuch, E., Mauldin, R. L., Lefer, B. L., Shetter, R. E., and Dibb, J. E.: Measurements of pernitric acid at the South Pole during ISCAT 2000, Geophys. Res. Lett., 29, 2011, doi:10.1029/2002gl015703, 2002.

Sobanski, N., Tang, M. J., Thieser, J., Schuster, G., Pöhler, D., Fischer, H., Song, W., Sauvage, C., Williams, J., Fachinger, J., Berkes, F., Hoor, P., Platt, U., Lelieveld, J., and Crowley, J. N.: Chemical and meteorological influences on the lifetime of NO_3 at a semi-rural mountain site during PARADE, Atmos. Chem. Phys., 16, 4867–4883, doi:10.5194/acp-16-4867-2016, 2016.

Thaler, R. D., Mielke, L. H., and Osthoff, H. D.: Quantification of nitryl chloride at part per trillion mixing ratios by thermal dissociation cavity ring-down spectroscopy, Anal. Chem., 83, 2761–2766, doi:10.1021/ac200055z, 2011.

Thieser, J., Schuster, G., Schuladen, J., Phillips, G. J., Reiffs, A., Parchatka, U., Pöhler, D., Lelieveld, J., and Crowley, J. N.: A two-channel thermal dissociation cavity ring-down spectrometer for the detection of ambient NO_2, RO_2NO_2 and $RONO_2$, Atmos. Meas. Tech., 9, 553–576, doi:10.5194/amt-9-553-2016, 2016.

Voigt, S., Orphal, J., and Burrows, J. P.: The temperature and pressure dependence of the absorption cross-sections of NO_2 in the 250-800 nm region measured by Fourier-transform spectroscopy, J. Photoch. Photobio. A, 149, 1–7, doi:10.1016/s1010-6030(01)00650-5, 2002.

Wayne, R. P., Barnes, I., Biggs, P., Burrows, J. P., Canosa-Mas, C. E., Hjorth, J., Le Bras, G., Moortgat, G. K., Perner, D., Poulet, G., Restelli, G., and Sidebottom, H.: The nitrate radical: Physics, chemistry, and the atmosphere, Atmos. Environ. A-Gen., 25, 1–206, 1991.

Wild, R. J., Edwards, P. M., Dube, W. P., Baumann, K., Edgerton, E. S., Quinn, P. K., Roberts, J. M., Rollins, A. W., Veres, P. R., Warneke, C., Williams, E. J., Yuan, B., and Brown, S. S.: A measurement of total reactive nitrogen, NO_y, together with NO_2, NO, and O_3 via cavity ring-down spectroscopy, Environ. Sci. Technol., 48, 9609–9615, doi:10.1021/es501896w, 2014.

Wooldridge, P. J., Perring, A. E., Bertram, T. H., Flocke, F. M., Roberts, J. M., Singh, H. B., Huey, L. G., Thornton, J. A., Wolfe, G. M., Murphy, J. G., Fry, J. L., Rollins, A. W., LaFranchi, B. W., and Cohen, R. C.: Total Peroxy Nitrates (ΣPNs) in the atmosphere: the Thermal Dissociation-Laser Induced Fluorescence (TD-LIF) technique and comparisons to speciated PAN measurements, Atmos. Meas. Tech., 3, 593–607, doi:10.5194/amt-3-593-2010, 2010.